Journal of Electroanalytical Chemistry 896 (2021) 115331

Contents lists available at ScienceDirect

Journal of Electroanalytical Chemistry

journal homepage: www.elsevier.com/locate/jelechem

Anodic coulometry of zero-valent iron nanoparticles

Annelis O. Sánchez-Álvarez [a,*], Jeffrey E. Dick [b,c], Eduardo Larios [d], Carlos R. Cabrera [a,*]

[a] Department of Chemistry, University of Puerto Rico, Río Piedras Campus, San Juan, PR 00931, USA
[b] Department of Chemistry, The University of North Carolina at Chapel Hill, NC 27599, USA
[c] Lineberger Comprehensive Cancer Center, School of Medicine, The University of North Carolina at Chapel Hill, Chapel Hill, NC 27599, USA
[d] Departamento de Ingeniería Química y Metalurgia, Universidad de Sonora, Hermosillo, 83000, México

ARTICLE INFO

Keywords:
Electrochemistry
Collision
Nanoscale zero-valent iron (nZVI)
Magnetite (Fe_3O_4)
Nanoparticle sizing
Anodic particle coulometry (APC)
Transmission electron microscopy (TEM)
Electron energy loss spectroscopy (EELS)

ABSTRACT

Nanoscale zero-valent iron (nZVI) particles are currently used for environmental remediation due to their ion sequester ability. This trait plus their magnetic behavior, and biocompatibility, makes them a promising alternative for heavy metal poisoning treatment, development of MRI dye, and drug delivery loads, among others. Their rapid passivation in aqueous media inhibit their differentiation from magnetite (Fe_3O_4) by electrochemical methods, due to its surface oxide. Herein, this work is focused on applying the electrochemical method known as anodic particle coulometry (APC) to detect and characterize nZVI. During the experiments, current blips are observed as a result of a current increase when the electroactive nZVI particle reaches the Au working ultra-microelectrode surface. The integration of current blips resulted in a charge distribution between 4 pC and 5 pC, which correlates with nanoparticles in a size range between 70 nm and 100 nm. The size distribution obtained were compared to the size distribution found using scanning transmission electron microscopy (STEM) and nanoparticle tracking analysis (NTA). The results were compatible with the results obtained by the other two techniques. Characterization of nZVI particles using x-ray photoelectron spectroscopy (XPS) and electron energy loss spectroscopy (EELS) validate the presence of elemental iron which differentiates the material from magnetite. A chemical shift of ca. 1 eV from metallic iron to iron oxide (L_3: 708 eV and L_2: 721.2 eV versus L_3: 709 eV and L_2: 722.2 eV) is observed from EELS at nZVI particle center and edge, respectively. This suggests the presence of a passivated surface and a metallic core, a metallic core and oxide shell structure.

1. Introduction

Advances in single metal nanoparticle detection [1–12], soft particles in non-homogeneous solutions [4,13–21], and the detection of one atom and clusters of atoms [1–4,16,19–24], are examples of promising accomplishments in single nanoparticle collision chemistry. The study of single particle electrochemistry is important to understand differences in chemical and physical properties of single particles as opposed to data obtained by ex-situ measurements [25,26]. Furthermore, in terms of analysis, the specific detection of single particles achieves the ultimate sensitivity: a limit of detection of a single particle.

Single Particle Detection (SPD) methods have emerged as an electrochemical alternative for nanoparticle (NP) characterization [27]. This novel electrochemistry method has obtained remarkable development in recent years. Nevertheless, NP are mostly characterized by transmission electron microscopy (TEM) or by spectroscopic methods [1,21,22]. New methods, as SPD, are needed since NPs are nanomaterials that have shown size dependent in optical properties and surface reactivity and have a wide range of applications, from drug delivery to environmental nanotechnology. Characterization of NP using SPD methods is a wide field to be explored and developed. This analytical method may be applied in different nanomaterials in many research fields. Herein, this work shows the characterization of nanoscale zero-valent iron (nZVI) particles using anodic particle coulometry (APC) for the first time. APC can be successfully used to identify particles with similar electrochemical properties, and accurately offers data according to the material appearance. This advantage makes possible the obtaining of data that reflects a characteristic “print”, which can be used to differentiate between materials with similar electrochemical properties but different physical semblance. During the electrochemical oxidation of nZVI particles in dilute solutions, anodic current blips were observed as a result of a current increase when the electroactive nZVI particle reached the Au ultramicroelectrode sur-

* Corresponding authors.
E-mail addresses: annelis.sanchez@upr.edu (A.O. Sánchez-Álvarez), carlos.cabrera2@upr.edu (C.R. Cabrera).

https://doi.org/10.1016/j.jelechem.2021.115331
Received 26 October 2020; Received in revised form 29 April 2021; Accepted 2 May 2021

face. Because of their magnetic trait, nZVI particles present poor dispersion which makes it difficult to use techniques such as dynamic light scattering (DLS). APC gives an insight on the sample´s distribution, permitting the measuring of one nZVI particle, but also suggesting the agglomeration and chain formation that occurs within the sample. This ability compares with the advantage of using microscopic techniques that gives observable data, an image. The obtained results strengthen and validates the advantages given by this electrochemical technique when using materials of diverse properties, in this case a magnetic electroactive particle.

NZVI particles are known to be ion sequesters and are used for environmental remediation [28–30]. Due to their ion sequester ability, magnetic behaviour, and biocompatibility, nZVI particles are a promising alternatives for heavy metal poisoning remediation [31]. NZVI particles has shown to decrease the toxicity in heavy metal poisoned soils and waters, being able to clean water from chlorinated compounds with almost 100% efficiency [32–36]. Recently, Soto-Hidalgo et al. has shown its use in contaminated soil from Cienaga las Cucharillas, Cataño, Puerto Rico [42].

2. Material and methods

All chemicals used were of high purity and used as received. Reagents and solvents used during these experiments such as: $FeCl_3 \cdot 6H_2O$, $NaBH_4$, KCl, NaH_2PO_4, Na_2HPO_4, $K_4Fe(CN)_6 \cdot 3H_2O$, highly pure ethanol, and Whatman membrane filters nylon pore ≤ 1 μm, were bought from Millipore Sigma (Sigma Aldrich). The iron (II,III) oxide (magnetite) nanopowder used was obtained from Fisher Scientific and manufactured by Alfa Aesar. The grids used for TEM and EELS samples were made of a carbon thin film over copper by Cornell Center for Material Research (CCMR). The UMEs used for these experiments were prepared by Annelis Sánchez under the supervision of Dr. Allen J. Bard´s group at The University of Texas at Austin.

2.1. nZVI particles synthesis

nZVI particles were synthesized following the Zhang et al. synthesis via reduction of Fe^{3+} [35]. Briefly, approximately 1.36 g of $FeCl_3 \cdot 6H_2O$ (5 mmol) were dissolved in 30 mL of a 1:5 water/ethanol solution. The reducing agent was prepared by dissolving 3.03 g of $NaBH_4$ in 100 mL of water (the $NaBH_4$ excess is to accelerate the synthesis reaction) [37]. The reductive titration was settled at a 65 drops per minute rate, at room temperature, and with continuous vigorous agitation. Stirring continued for at least 30 min after the titration was finished. The nZVI nanoparticles synthesis occurs via the following reaction:

$$4Fe^{3+} + 3BH_4^- + 9H_2O \rightarrow 4\,Fe^0 \downarrow + 3H_2BO_3^- + 12H^+ + 6H_2 \quad (1)$$

The particles were then filtered using a vacuum filtration system and a 0.1 μm size pore filter paper. The obtained particles were thoroughly washed with highly pure ethanol to remove the salts and other adsorbed ions and was left for drying at the filtration system for at least 20 min after the ethanol wash. Particles were stored in a vial sealed with parafilm, under vacuum condition, inside a desiccator to prevent oxidation from the environment.

2.2. X-ray photoelectron spectroscopy analysis (XPS)

X-ray photoelectron spectroscopy (XPS) analysis was done using a PHI Physical Electronics 5600ci ESCA System with a Mg Kα monochromatic X-ray source (350 W) and a hemispherical electron energy analyzer. All binding energies shown have been calibrated during data analysis using C (1 s) binding energy peak at 284.8 eV [38].

2.3. Electron energy loss spectroscopy (EELS)

Electron energy loss spectroscopy (EELS) was done using a FEI Monochromated 200 kV Tecnai TF20 STEM at the Cornell Center for Material Research (CCMR), Cornell University.

2.4. Nanoparticle tracking analysis (NTA)

Nanoparticle tracking analysis (NTA) was used to characterize the nZVI nanoparticles. A 80 pM aqueous solution of nZVI nanoparticles in 100 mM KCl (Sigma Aldrich) was prepared and sonicated for 25 min to improve particle dispersion. The solution was further diluted by 12.5x using 100 mM KCl and analyzed using a NANOSIGHT Version 2.3.

2.5. Transmission electron microscopy (TEM)

Transmission electron microscopy (TEM) images were obtained using a FEI Tecnai T12 BioTwin 120 kV TEM and FEI Tecnai G2F20 200 kV TEM/STEM at Cornell Center for Material Research (CCMR) facilities. The 80 pM nZVI stock solution was analyzed before and after exposure to sonication in 200 mM phosphate buffer at pH = 10 for at least 30 min. Diluted samples were analyzed after exposure to APC treatment. The TEM grids used for these samples were made of a carbon thin film over copper.

2.6. Anodic linear sweep voltammetry (ASV)

Several glassy carbon electrodes, with 3 mm in diameter, were cleaned to a mirror-like finish by smooth polishing with 1 μm, 0.3 μm, and 0.1 μm alumina for 3 min and thorough washing with nanopure water with a resistivity of 18.2 Ω-cm. The cleaned glassy carbon electrodes, before being surface modified, were treated, to avoid hydrophilicity, by holding a reducing potential for 5 min under continuous nitrogen bubbling. The electrodes were then modified with either a nZVI ink or Fe_3O_4 ink, via 5 μL drop cast, and allowing the electrodes air dry overnight. The inks were prepared by using a mixture of 500 μL of Nano pure water + 125 μL of 2-propanol + 5 μL of 10% Nafion perfluorinated ion-exchange resin from Sigma Aldrich + 1.0 mg of the iron material (nZVI nanoparticles or Fe_3O_4), and 25 min sonication before the drop casting procedure. The magnetite (Fe_3O_4) nanoparticles used in this work were lower than 50 nm particle size, commercially available from Alfa Aesar as a powder. The ASV was done using a 3 electrodes glass cell with a Pt wire as counter, Ag/AgCl (3 M KCl) as reference, and bare and modified glassy carbon working electrodes. The ASV conditions used were; 10 s equilibrium time and 0.01 V/s potential scan rate from −0.2 V to 0.6 V potential window. These measurements were done in a 200 mM phosphate buffer solution at pH 10.

2.7. Anodic particle coulometry (APC)

The instrument used for these analyses was a CHI 6044E Electrochemical Analyzer with picoamp buster and a faraday cage. This setup provides current range between ± 10 pA to ± 0.25 A in 12 ranges. In addition, the current resolution is 0.0015% of current range, with a minimum current resolution of 0.3 fA (CH Instruments, Inc.).

The technique used for this analysis was chronoamperometry, i.e. current (i) vs. time (t) curves. The electrochemical cell system was a 3 electrodes cell using a 12.5 Au ultra-microelectrode (UME) as the working, Pt wire as a counter, and Ag/AgCl (3 M KCl) as the reference electrodes.

A modified version of Tschulik et al. [39] was used for this analysis. Briefly, 15 mL of 80 pM nZVI stock aqueous solution was prepared using 200 mM phosphate buffer at pH 10 as the solvent and sonicating for 20–30 min before further dilutions. After sonication, dilutions of 1.00 pM, 0.75 pM, 0.50 pM, and 0.25 pM were prepared using the

same phosphate buffer as the aqueous solvent, followed by a step of at least 20 min sonication or until samples were ready to be analyzed. Samples were analyzed starting with the lowest concentration (0.25 pM) up to the most concentrated (1.00 pM) nZVI solutions. The Au UME behaviour was evaluated by cyclic voltammetry (CV) with a standard solution of 15 mM $K_4Fe(CN)_6{\cdot}3H_2O$ between each chronoamperometric run.

3. Results and discussion

3.1. Materials characterization

3.1.1. X-ray photoelectron spectroscopy analysis

Freshly prepared nZVI particles were analyzed by X-ray photoelectron spectroscopy (XPS) to determine the elemental composition and oxidation state of the iron nanoparticles. The Fe $2p_{3/2}$ binding energy region for metallic iron appears between 706.7 and 707.1 eV, while peaks with a binding energy of 711.0 eV are associated to oxidized iron species [40]. The XPS analysis for nZVI showed a major contribution of Fe_3O_4 and FeOOH according to the Fe $2p_{3/2}$ peak found at 710.55 eV (see Fig. 1 and Fig. S1). These data correlates with previous characterization made by Sun et al. and Soto-Hidalgo et al. [37,41,42], where freshly prepared nZVI were analyzed obtaining Fe $2p_{3/2}$ binding energy peaks at 706 eV and 710.5 eV. Soto-Hidalgo et al. [41] attributed the peaks at 706.0 eV and 710.5 eV to the nZVI particle's metallic core and a passivation layer on the nZVI particle's surface, respectively. The highest binding energy was mainly attributed to Fe_3O_4 and FeOOH species due to iron oxidation upon atmospheric exposure [41]. The XPS spectrum (see Fig. 1) also showed a peak at 706.8 eV, attributed to Fe^0 in the nZVI particle's core. XPS is intrinsically surface sensitive hence the low Fe^0 contribution in the spectra since the nanoparticles are around 60–100 nm in diameter. The ΔE of 13.10 eV between Fe $2p_{3/2}$ and Fe $2p_{1/2}$ binding energy peak confirms the presence of Fe [37,41,43]. Deconvolution of the XPS spectrum and chi value are reported in Figs. S1 and S2. Major contribution of Fe^{2+} and Fe^{3+} are attributed to FeO, Fe_3O_4 and FeOOH species [43].

3.2. nZVI particle size determination

3.2.1. Nanoparticle tracking analysis (NTA)

The nZVI particles were analyzed using dynamic light scattering (DLS) (SI). The data suggested aggregation and poor dispersion (PDI value close to 1.00), mainly due to the nZVI behaviour of forming chain-like structures [37,41]. Nanoparticle tracking analysis (NTA) was done to achieve a better size measurement. NTA data (see Fig. 2) shows the majority of nZVI particles are between 69 nm and 89 nm, larger particles are also observed suggesting some agglomeration. From the NTA report, a mode of 69 nm, with an average of 92 nm, and a standard deviation of 47 nm were obtained. A total of six runs where done, each of which are based on an average of four internal runs. All six samples yielded similar results. The NTA data correlates with previous characterization analysis made by Sun et al. [37] using transmission electron microscopy (TEM), where the median and average size were determined to be 60.2 nm and 70.2 nm, respectively, with a standard deviation of 49.6 nm.

3.3. €Transmission electron microscopy (TEM) and electron energy loss spectroscopy (EELS)

To corroborate the size distribution of the nZVI particles, TEM analysis was also done (see Fig. 3). The data analysis of the nZVI particles showed a mode value of 60 nm, a median of 65 nm, and average of 67 nm, with a standard deviation of 28 nm. Moreover, TEM images were done after sonication of the nZVI 80 pM stock aqueous solution for at least 30 min as well as APC treated samples. Due to the nature of the experiments, even the most concentrated stock solution (80 pM) was highly diluted. Therefore, high concentration of salt from the phosphate buffer aqueous solution were observed (see Figs. S3 and S4). However, the 80 pM stock solution showed the presence of branched nanochains (see Figs. S3 and S4). High-angle annular dark-field imaging (HAADF) of the nanochain showed a difference in contrast between the metallic iron core center (brighter) and outer shell iron oxide (less contrast) (see Fig. 4). A Fourier transform (FTT) analysis of the HRTEM image showed several interplanar distances: 4.95 Å, 3.15 Å, 2.07 Å, and 1.37 Å (see Fig. 5). The 2.07 Å and 1.37 Å interplanar distances correspond to the Fe^0 core (ICSD 98–004-4863), while the interplanar distances of 4.95 Å and 2.96 Å correspond to magnetite, Fe_3O_4, (ICSD 98–008-2441) [44]. This confirms the presence of a metallic iron core and a Fe_3O_4 surface. This is also in agreement with Sun et al. finding about the persistence of a substantial metallic core even though the presence of a passivated surface [37]. The X-ray absorption near edge structure (XANES) analysis by Sun et al. suggests 42% Fe^0 is maintained even after six weeks of water exposure [37]. In fact, the surface passivation works as a protective shield, decreasing iron's oxidation rate as the oxidized layer grows. Energy dispersive X-ray spectroscopy (EDS) line scan analysis of the

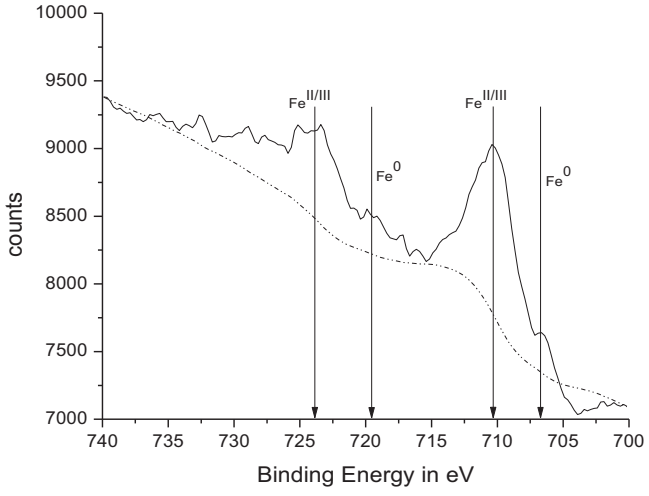

Fig. 1. X-ray photoelectron spectroscopy spectrum of the Fe 2p binding energy region of the freshly prepared nZVI nanoparticles, showing the presence of different iron oxidation states.

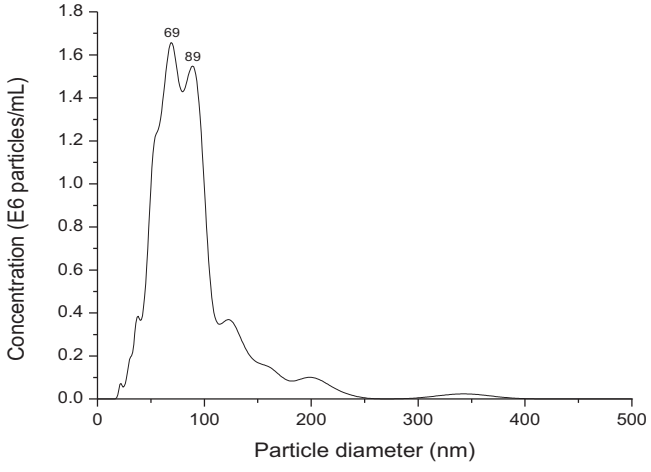

Fig. 2. Nanoparticle tracking analysis (NTA) data of nZVI in 0.1 M KCl obtained with the Nanosight instrument.

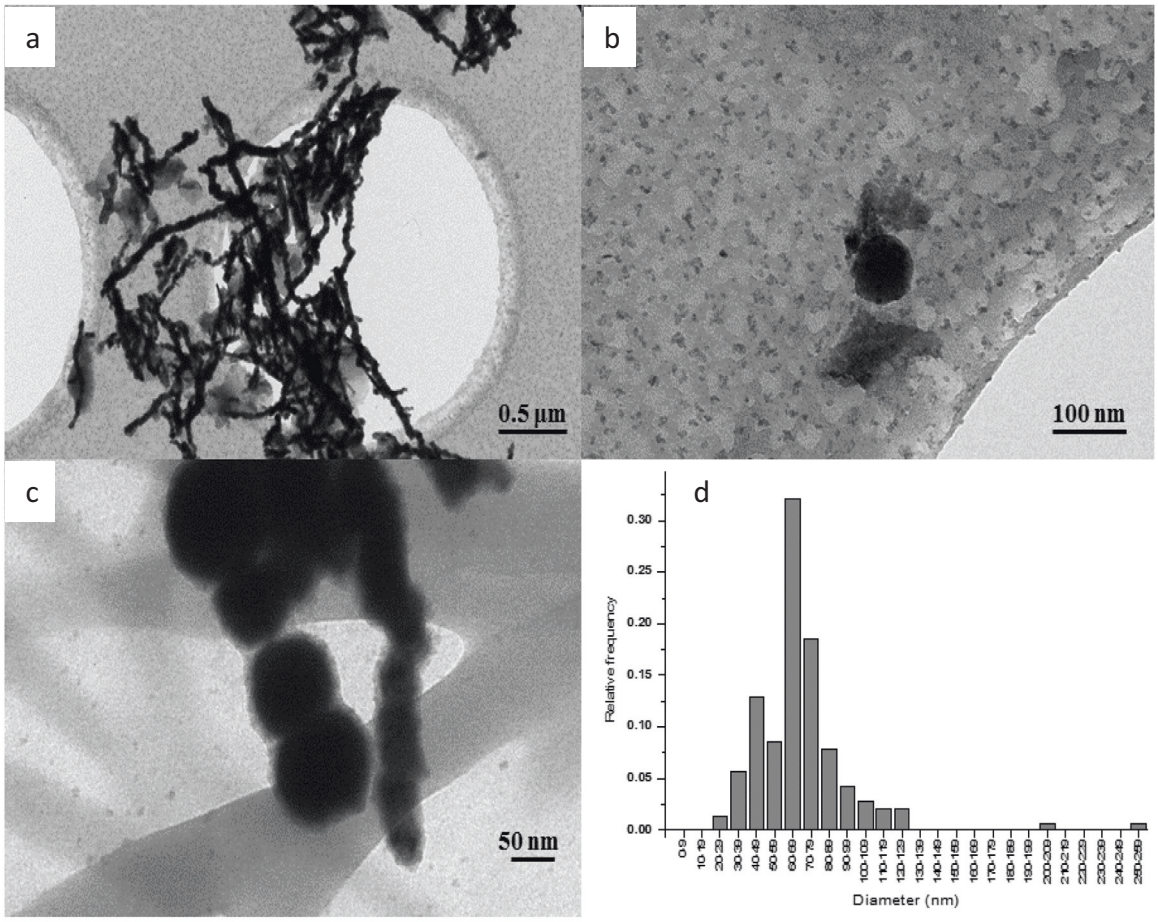

Fig. 3. (a-c) TEM images and (d) size distribution of as synthesized nZVI. Size distribution is based on a total of 140 particles. The relative frequency was calculated by dividing per the total number of nZVI particles. TEM images scale are (a) 0.5um, (b) 100 nm, and (c) 50 nm. (d) Histogram of particle sizes was plotted as relative frequency versus particle diameter.

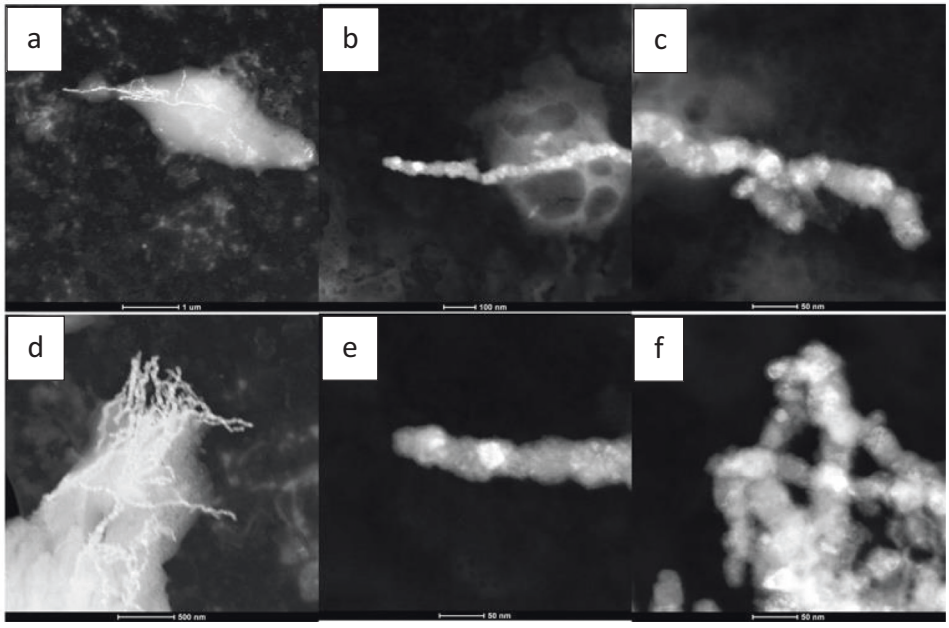

Fig. 4. High-angle annular dark-field imaging (HAADF) of 80 pM stock solution which were exposed for at least 30 min of sonication in 200 mM phosphate solution at pH 10. TEM images scale: (a) 1 µm, (b) 100 nm, (c) 50 nm, (d) 500 nm, (e) 50 nm, and (f) 50 nm.

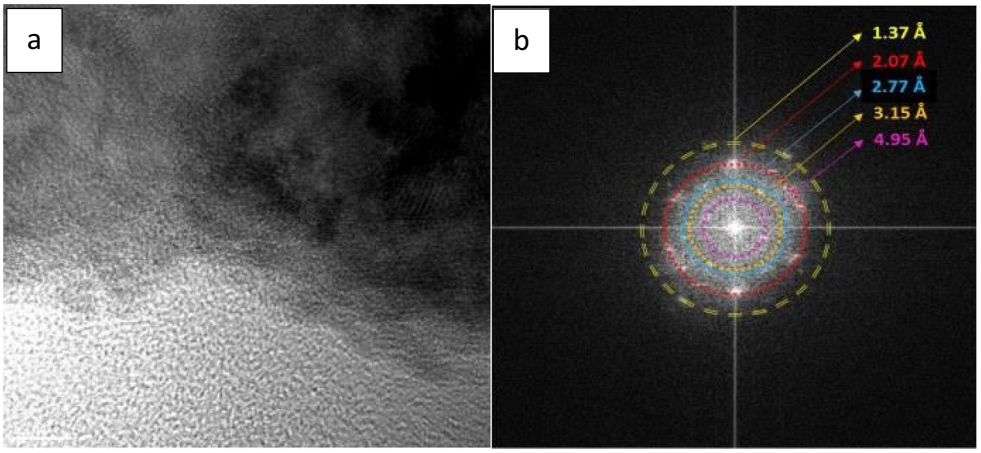

Fig. 5. (a) HRTEM image and (b) Fast Fourier transform (FTT) analysis on NZVI TEM images. HRTEM image not neat due to high concentration of salts and carbon grid presence.

TEM images also supports the presence of a metallic core–shell of passivation (see Figs. S5 and S6). This branched nanochains were not observed in the APC treated samples, perhaps because of the salt-to-sample concentration ratio or the complete oxidation of the sample.

The freshly prepared nZVI particles were analyzed using EELS to confirm its elemental composition. The EELS was done at different regions of the nZVI particles: center and edge. Metallic iron bands were observed at the center of the nZVI particle, while both iron and oxygen bands were observed at the edge. As demonstrated by Grunes et al. [45], EELS spectra of iron oxides show two peaks related to the oxygen K edge at 530 eV and 539 eV, the latter being the major contribution; and two peaks related to metallic iron $L_{3,2}$ edge at 706 eV and 719 eV, with an energy gap between the two white lines of 13.2 eV [46,47]. A detailed comparison between the different iron oxidation states using EELS technique done by Leapman et al. [47] shows a chemical shift of ~ 1.4 eV from metallic iron to iron oxides, a reduction of the white line width in the iron oxide, and an increase of the $I_{(L3)}/I_{(L2)}$ ratio intensity by a factor of 1.62 (from 3.4 to 5.5 after deconvolution) for the metallic iron to iron oxides ratio. The EELS spectra of nZVI particle, at the particle center (see Fig. 6), shows peaks at 708 eV and 721.2 eV corresponding to L_3 and L_2 of metallic iron. The energy gap between the white lines was 13.2 eV, in agreement with the value published by Grunes et al. [45]. The absence of a peak in the 530–560 eV region of the EELS spectra at the nZVI particle center (black line) confirms a metallic core. At the edge of the nZVI particle, the EELS spectra (red lines) shows two peaks at 529.2 eV and 539.6 eV related to the oxygen K edge, confirming the nZVI particle passivated surface. A ca. 1 eV chemical shift from metallic iron to iron oxide (L_3: 708 eV, L_2: 721.2 eV vs. L_3: 709 eV, L_2: 722.2 eV) (Fig. 6 inset) is observed from nZVI center to edge EELSs. This is similar to the 1.4 eV shift stated by Leapman et al. for metallic iron vs. iron oxide [47]. A decrease in the white line width of the nZVI nanoparticle at the edge, and an increase of the intensity $I_{(L3)}/I_{(L2)}$ ratio by a factor of 1.61 (from 3.1 iron at the center to 5.0 iron at the edge) were also observed (see Table 1). This suggests a metallic core and passivated surface, also similar to the data obtained for metallic iron vs. iron oxide in previous works [45,47]. This EELS data correlates with the XPS analysis, and previous characterizations made by Sun et al. and Soto-Hidalgo et al. were the nZVI particle is described as having a metallic core and a passivated surface due to atmospheric exposure [37,41].

3.4. Electrochemical characterization

3.4.1. Linear sweep voltammetry (ASV)

Linear sweep voltammetry (see Fig. 7 and Fig. S7) was done to corroborate the redox electrochemical potential of the nZVI particles. In Fig. 7, linear sweep voltammograms were done with anodic current is taken as negative. The linear sweep voltammogram showed an oxidation peak at 0.30 V vs. Ag/AgCl for both: nZVI and Fe_3O_4. According to the Pourbaix diagram for iron in water, at pH 10, the mechanism of surface oxidize nZVI and Fe_3O_4 oxidation is [48]:

$$\boldsymbol{Fe_3O_4 + OH^- \rightarrow 3/2\ Fe_2O_3 + 1/2\ H_2O + e^-} \quad (2)$$

Since nZVI particles in aqueous media are surface oxide passivated, the oxidative mechanism is similar to that for magnetite ($Fe^{2+}Fe_2^{3+}O_4$). Therefore, it is not facile to electrochemically differentiate between nZVI and magnetite based on their redox potential.

4. Anodic particle coulometry (APC)

In this work, nZVI were electrochemically characterized using anodic particle coulometry (APC), by applying a 0.75 V overpotential for 300 s, as shown in Fig. 8 and Figs. S8–S10. The observed spikes of increasing current are representative of single collisions of the nZVI particles with the Au UME. This electrochemical technique is highly sensitive to particle size; therefore, is able to differentiate between particles of similar redox potentials based on their particle sizes. The technique consists of oxidizing one nanoparticle at a time, upon the nanoparticle collision with the Au UME surface. This collision of the nanoparticle on the electrode's surface will generate a current spike that is related to the particle's size by the following equation [39]:

$$r = \sqrt[3]{\frac{3MQ}{4\pi eNz\rho}}$$

Where r is the NP radius, M is the molar mass, Q is charge, e is electron charge, N is Avogadro's constant, z is the number of exchanged electrons, and ρ is nanoparticle density. Here, a homogeneous particle composition is assumed which is not precisely our case. However, is a good approximation.

For this electrochemical study, a series of solutions with different nZVI particle concentrations were used. nZVI aqueous solution of 0.25 pM, 0.50 pM, 0.75 pM, and 1.07 pM (where pM stands for moles of particles per L of solution) were used to compare the frequency of collision among them. The chronoamperometric current increased with concentration as well as the frequency of collisions (see Figs. 8 and S8). Notice the difference in current and steadiness of the chronoamperogram in absence of nZVI particles (see Fig. 8 (a)). No peak was observed in absence of nZVI particles. Each observed peak represents the oxidation of a nZVI particle while it collides on the Au UME's surface (see Fig. 8 (b)). In a previous work, Tschulik et al. [39] were able to characterize Fe_3O_4 nanoparticles with size range between 7 nm and 21 nm in radius (<50 nm diameter) using anodic

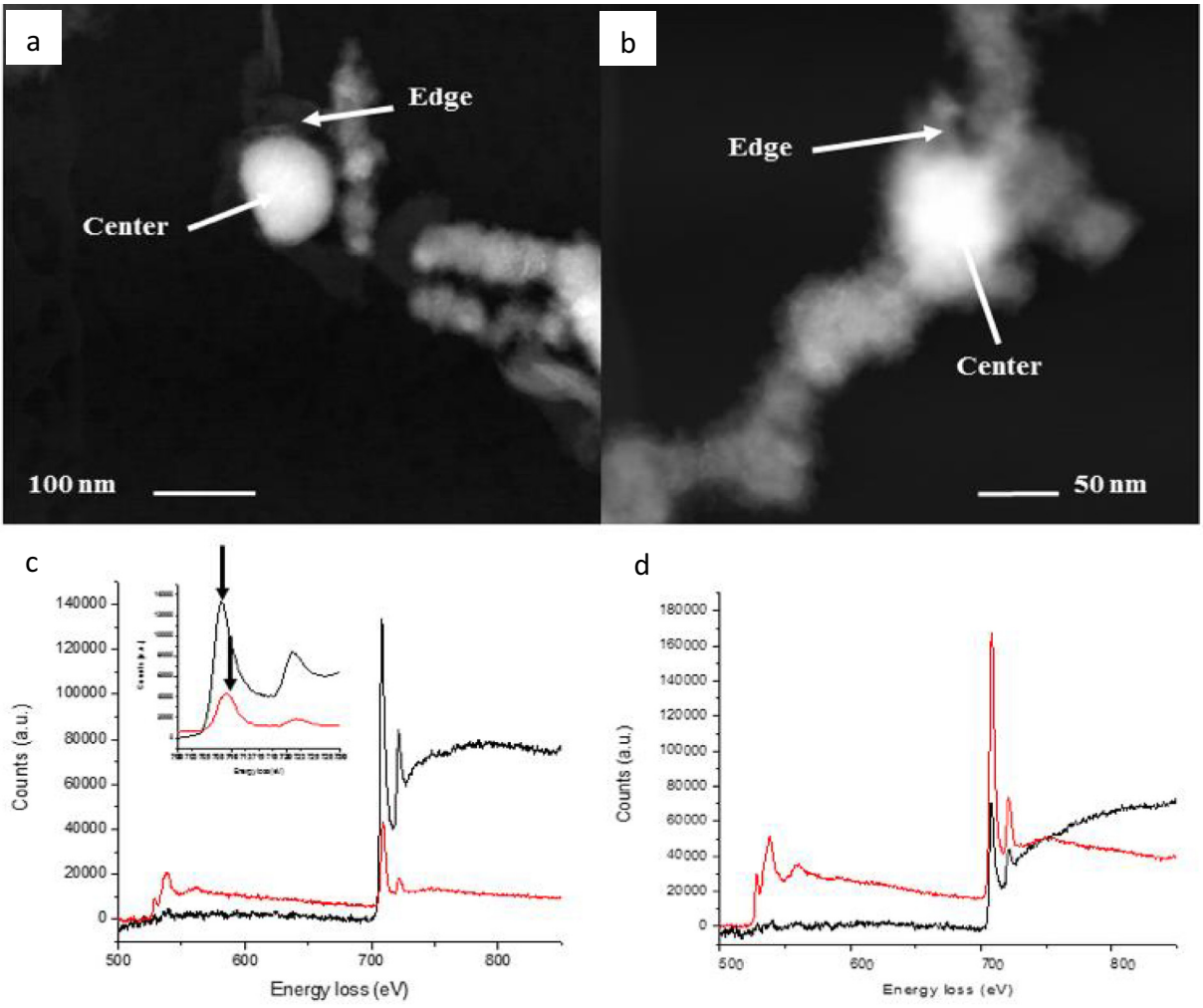

Fig. 6. Transmission electron microscopy image (a and b) and electron energy loss spectroscopy spectra (c and d) of two nZVI nanoparticles. The nZVI particles were analyzed by EELS at the center (black line) and edge-shell (red line) of the nanoparticle to compare their elemental composition. Inset showing the chemical shift and change in $I_{(L3)}/I_{(L2)}$ ratios between metallic iron and iron oxide.

Table 1
L_3 and L_2 energies, separation between abruption maximum (L_2-L_3), and intensity ratios (L_3/L_2) after deconvolution.

Fe Species	Energy (eV) L_3	Energy (eV) L_2	Energy difference respect to absorption maximum (eV)	Relative intensity ratio: L_3/L_2
Fe_{Center}	708.0	721.2	13.2	3.1
Fe_{Edge}	709.0	722.2	13.2	5.0

and cathodic particle coulometry. Herein nZVI particles having a >50 nm in diameter (60 nm − 90 nm size range) were used. The nZVI particles are magnetic, therefore, they were prompted to agglomerate [37,41]. The nZVI forms branched nanochain structures that can also collide with the electrode, in which case larger current blips are observed (see Figs. S8–S10). For example, comparably high current blips are seen close to 120 s and 50 s (see Fig. S8 (e), and Fig. S9 respectively), corresponding to collision of more than one nanoparticle. However, these larger blips are not representative of a single nZVI nanoparticle and were neglectable after *Z-test* statistical analysis of the samples. Sample dilution and sonication before APC analysis helped obtain single nanoparticle blips instead of agglomerated structures. Moreover, a branched nanochain structure is heavier than a single nZVI nanoparticle, increasing the chance of collision of the later one and settle down of the first one. Since blips due to agglomeration and formation of the nanochain structure are easier to be observed because of their size than the blip of a single nZVI nanoparticle, a detailed zoom in the current (i) versus time (t) graph was needed to quantize every collision.

Fig. 8 (A) shows a zoom in line (b) from 30 s to 100 s, circling peaks at 35 s and 95 s. Integration of these two peaks give a charge of ~10 pC each, corresponding to particles of ~112 nm. Appreciable smaller peaks between the marked peaks are observed corresponding to particles of smaller size (see Fig. 8 A). Additional data for other concentrations are shown in SI (see Figs. S8–S10).

In this work, ASV was done for both, nZVI particles larger than 50 nm and Fe_3O_4 nanoparticles smaller than 50 nm in diameter. The nanoparticles were not easily differentiable by this electrochemical technique. However, using APC the nZVI particle data (see Fig. 9) shows a majority of charge distribution between 4 pC − 5 pC, which

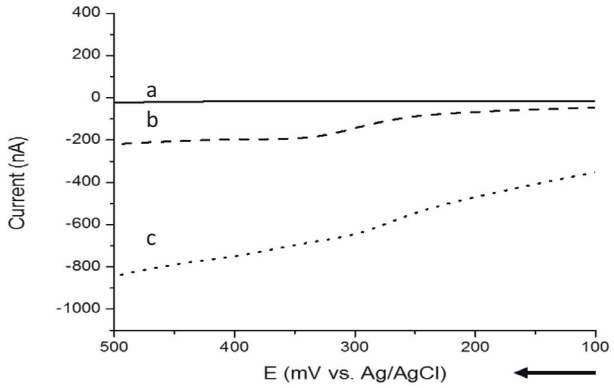

Fig. 7. Linear sweep voltammetry of a (a) clean glassy carbon (GC), (b) nZVI modified GC, and (c) Fe_3O_4 modified GC electrodes; in ~ 0.2 M phosphate buffer at pH 10 and a 0.01 V/s scan rate (arrow shows direction of potential scan), quiet time for 10 s. Complete CV data are shown in SI.

correlates with nanoparticles in a size range between 70 nm and 100 nm. The size distribution analysis showed that the majority of particles are the range of 80 nm − 89 nm, similar to the results obtained by NTA technique. The average size was determined to be 102 nm, while the median and mode were both at 89 nm, with a standard deviation of 35 nm. The data obtained using the lowest nZVI concentration reflects similar average and median (88 nm) but a reduction in the standard deviation (±12 nm), suggesting better electrochemical results when using lower concentrations. The nZVI particle size values obtained by APC are comparable to the values obtained by NTA and TEM. These results are compared in Fig. 10 and clearly sustains the validity of the electrochemical technique for single particle analysis and size determination. The APC analysis done by Tschulik et al. [39] to magnetite (Fe_3O_4) nanoparticles with lower than 50 nm diameter showed a charge distribution with a modal of 0.012 pC, correlating with a particle with a 11 nm radius and with a standard deviation of ± 4 nm. Both results suggest that APC is able to differentiate between nZVI nanoparticles and magnetite (Fe_3O_4) nanoparticles of different sizes, something not facile for other electrochemical techniques.

A frequency vs. concentration analysis of the nZVI particles using APC experiments (see Fig. 11) show a lineal relationship for the first concentrations (0.25 pM – 0.75 pM), with a R^2 = 0.9758, while it deviates from linearity with a higher nZVI concentrated solution (1.0 pM) (see Fig. 11, inset). This may be due to the passivation of the electrode surface which leads to efficiency decay, higher distribution of nZVI particle agglomerations as the concentration increases, or larger magnetic effects by nZVI particles. Moreover, the slope of the line was used to calculate the nanoparticle's diffusion coefficient (D_{NP}) by rearrangement of the equation:[2]

$$f = 4DNPCNPNArelec \quad (4)$$

where f is the frequency of collisions based on diffusion, D_{NP} is the nanoparticle's diffusion coefficient, C_{NP} is the nanoparticle's concentration, N_A is Avogadro's number, and r_{elec} is the electrode's radius.

This value was compared to the nanoparticle's diffusion coefficient obtained from Stokes-Einstein's equation [49]:

$$D_{NP} = \frac{k_B T}{6\pi\eta r_{NP}} \quad (5)$$

where D_{NP} is the nanoparticle's diffusion coefficient, k_B is Boltzmann constant, T is temperature, η is viscosity of solution, and r_{NP} is the nanoparticle's radius.

The values were 3.10 × 10^{-8} cm^2/s and 5.84 × 10^{-8} cm^2/s, respectively. The magnitude of the diffusion coefficient and correlation of both values sustain the idea of single nanoparticles colliding on the electrode's surface.

5. Conclusions

The single particle collision experiment, using APC technique, was able to detect the nZVI particle sizes that correlated with TEM and NTA techniques. For the first time, APC was used to characterize nZVI particles and the results shows good correlation with the size obtained using other methods such as microscopy and spectroscopy. These

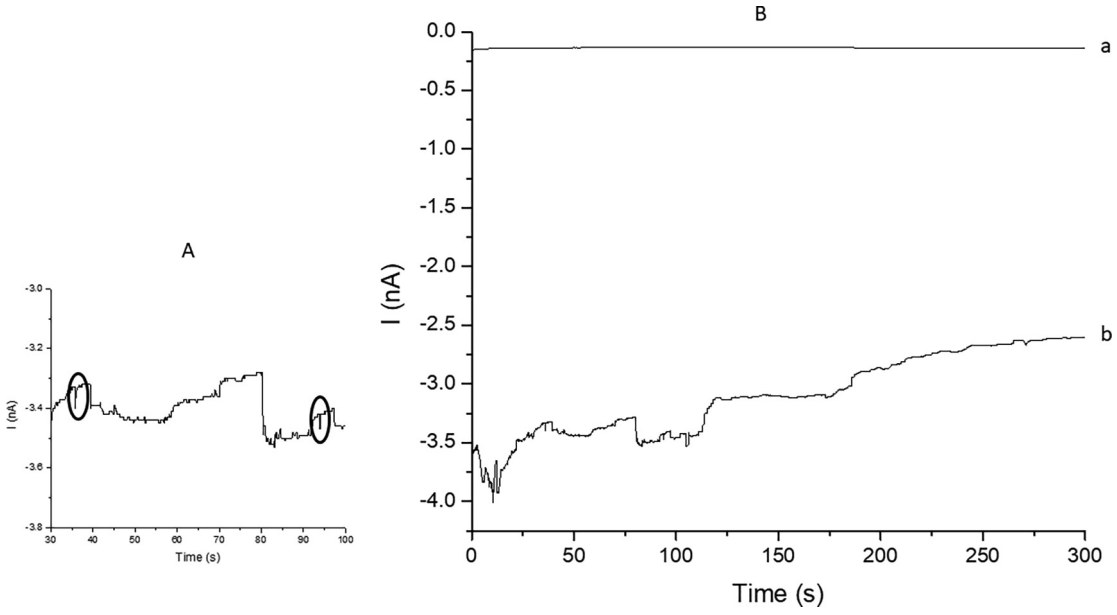

Fig. 8. Amperometric current (i) vs. time (t) curve of: 200 mM phosphate buffer without (a), and with 0.25 pM nZVI particles (b) in 200 mM phosphate buffer at pH 10. An applied potential of 0.75 V vs. Ag/AgCl (3 M KCl) for 300 s was used. The measurement was done using a 12.5 μm Au UME working electrode, Pt wire counter electrode, and Ag/AgCl (3 M KCl) reference electrode. Zoom in line b shows collision between 30 s and 100 s, circling peaks at 35 s and 95 s (A).

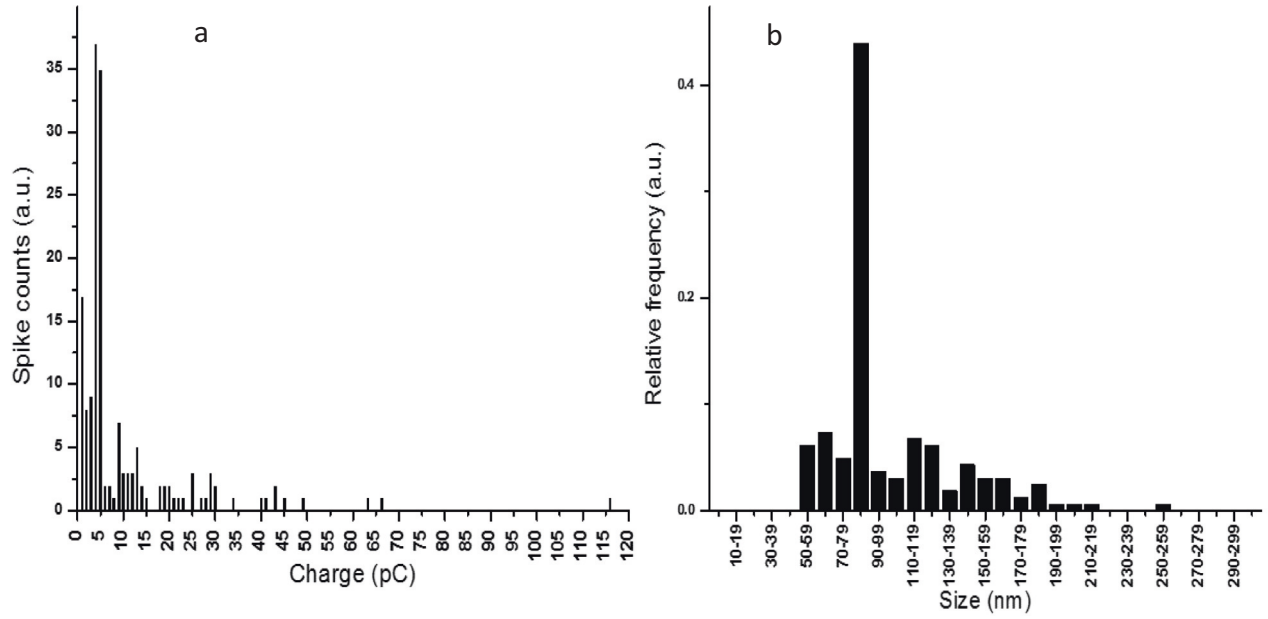

Fig. 9. nZVI collision experiments data analysis after *z* test: (a) charge distribution from 0 to 120 pC and (b) size distribution from 0 to 290–299 nm of nZVI particles. OriginPro 8.6 for the peak current integration.

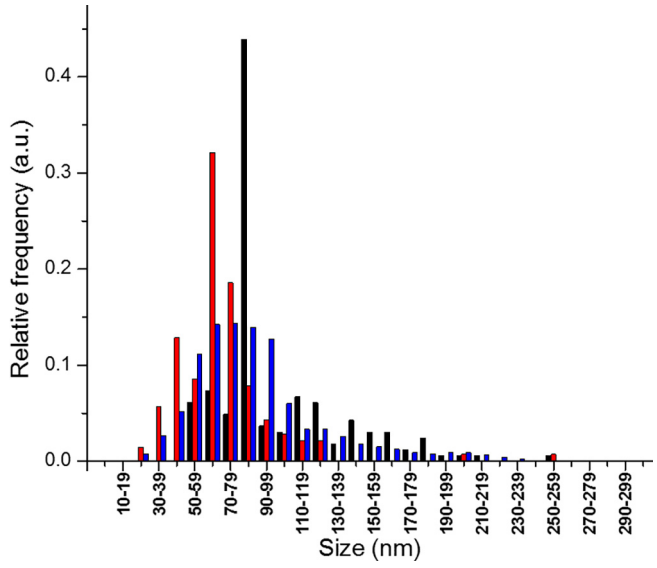

Fig. 10. nZVI size distribution comparison with data from anodic particle coulometry (APC) (black), transmission electron microscopy (TEM) (red), and Nanoparticle tracking analysis (NTA) (blue).

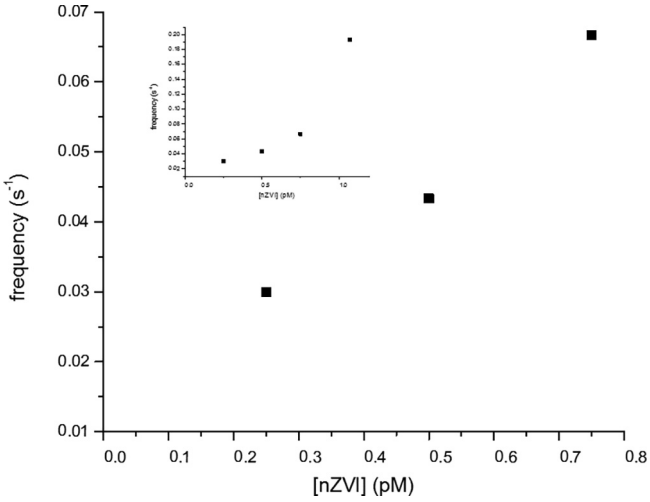

Fig. 11. nZVI particle collision frequency versus nZVI concentration, in pM, from the APC data. Inset for the [nZVI] range between 0 and 1.25 pM. The collision measurements were done using a 12.5 μm Au UME working, Pt wire counter, and Ag/AgCl (3 M KCl) reference electrodes.

experiments not only validate the technique, but also suggest the use of APC to differentiate between materials with similar electrochemical behaviours that differ in size; a new perspective to be used in heavy metal remediation by nZVI. Single particle techniques are promising in environmental nanotechnology applications due to the high sensitivity that they offer. However, many environmental samples are very complex. Several organic molecules may have similar electrochemical behaviours, for such is an increased value if the technique can not only detect but confirm its specificity by size exclusion or chromatography. The concentration range where the technique has an optimum performance is also something to be considered and explored from sample to sample. Moreover, this technique may allow to sense nZVI particles at ultralow concentration at sites where it is use for water remediation.

CRediT authorship contribution statement

Annelis O. Sánchez-Álvarez: Conceptualization, Data curation, Formal analysis, Investigation, Methodology, Project administration, Software, Visualization, Writing original draft, writing review & editing. **Jeffrey E. Dick:** Supervision, Validation, Review & editing. **Eduardo Larios:** Formal analysis of HAADF, HRTEM, FTT, and EDS. **Carlos R. Cabrera:** Funding acquisition, Project administration, Resources, Supervision, Validation, Writing-review & editing.

Declaration of Competing Interest

The authors declare that they have no known competing financial interests or personal relationships that could have appeared to influence the work reported in this paper.

Acknowledgements

This work was supported by NSF-CREST Grant Number 1736093. AOS was supported by NIH-RISE Fellowship Grant No. 5R25GM061151-15. The authors are grateful to Dr. Richard M. Crooks and Dr. Alma Castaneda (University of Texas at Austin) for the use of the Nanosight Instrument and Dr. Mariena Silvestry-Ramos (Cornell University) for TEM images and EELS. The use of the Cornell Center for Materials Research Shared Facilities, which are supported through the NSF MRSEC grant number DMR-1719875, are greatly appreciated.

Appendix A. Supplementary data

Supplementary data to this article can be found online at https://doi.org/10.1016/j.jelechem.2021.115331.

References

[1] X. Xiao, F.-R. Fan, J. Zhou, A.J. Bard, Current Transients in Single Nanoparticle Collision Events, J. Am. Chem. Soc. 130 (49) (2008) 16669–16677.
[2] J.E. Dick, A.T. Hilterbrand, A. Boika, J.W. Upton, A.J. Bard, Electrochemical detection of a single cytomegalovirus at an ultramicroelectrode and its antibody anchoring, Proc. Natl. Acad. Sci. 112 (17) (2015) 5303–5308.
[3] B.-K. Kim, A. Boika, J. Kim, J.E. Dick, A.J. Bard, Characterizing Emulsions by Observation of Single Droplet Collisions—Attoliter Electrochemical Reactors, J. Am. Chem. Soc. 136 (13) (2014) 4849–4852.
[4] M. Zhou, J.E. Dick, A.J. Bard, Electrodeposition of Isolated Platinum Atoms and Clusters on Bismuth—Characterization and Electrocatalysis, J. Am. Chem. Soc. 139 (48) (2017) 17677–17682.
[5] J. Kim, B.-K. Kim, S.K. Cho, A.J. Bard, Tunneling Ultramicroelectrode: Nanoelectrodes and Nanoparticle Collisions, J. Am. Chem. Soc. 136 (23) (2014) 8173–8176.
[6] A. Boika, A.J. Bard, Time of First Arrival in Electrochemical Collision Experiments as a Measure of Ultralow Concentrations of Analytes in Solution, Anal. Chem. 87 (8) (2015) 4341–4346.
[7] S.J. Kwon, H. Zhou, F.-R.-F. Fan, V. Vorobyev, B. Zhang, A.J. Bard, Stochastic electrochemistry with electrocatalytic nanoparticles at inert ultramicroelectrodes —theory and experiments, Phys. Chem. Chem. Phys. 13 (12) (2011) 5394–5402.
[8] H.S. Ahn, A.J. Bard, Single-Nanoparticle Collision Events: Tunneling Electron Transfer on a Titanium Dioxide Passivated n-Silicon Electrode, Angew. Chem. Int. Ed. 54 (46) (2015) 13753–13757.
[9] J.H. Park, S.N. Thorgaard, B. Zhang, A.J. Bard, Single particle detection by area amplification: single wall carbon nanotube attachment to a nanoelectrode, J. Am. Chem. Soc. 135 (14) (2013) 5258–5261.
[10] X. Xiao, S. Pan, J.S. Jang, F.-R.-F. Fan, A.J. Bard, Single Nanoparticle Electrocatalysis: Effect of Monolayers on Particle and Electrode on Electron Transfer, J. Phys. Chem. C 113 (33) (2009) 14978–14982.
[11] J.H. Park, A. Boika, H.S. Park, H.C. Lee, A.J. Bard, Single Collision Events of Conductive Nanoparticles Driven by Migration, J. Phys. Chem. C 117 (13) (2013) 6651–6657.
[12] X. Xiao, A.J. Bard, Observing Single Nanoparticle Collisions at an Ultramicroelectrode by Electrocatalytic Amplification, J. Am. Chem. Soc. 129 (31) (2007) 9610–9612.
[13] J.E. Dick, C. Renault, B.-K. Kim, A.J. Bard, Simultaneous Detection of Single Attoliter Droplet Collisions by Electrochemical and Electrogenerated Chemiluminescent Responses, Angew. Chem. Int. Ed. 53 (44) (2014) 11859–11862.
[14] J.E. Dick, E. Lebègue, L.M. Strawsine, A.J. Bard, Millisecond Coulometry via Zeptoliter Droplet Collisions on an Ultramicroelectrode, Electroanalysis 28 (10) (2016) 2320–2326.
[15] J.E. Dick, A.T. Hilterbrand, L.M. Strawsine, J.W. Upton, A.J. Bard, Enzymatically enhanced collisions on ultramicroelectrodes for specific and rapid detection of individual viruses, Proc. Natl. Acad. Sci. 113 (23) (2016) 6403–6408.
[16] M.W. Glasscott, J.E. Dick, Direct Electrochemical Observation of Single Platinum Cluster Electrocatalysis on Ultramicroelectrodes, Anal. Chem. 90 (13) (2018) 7804–7808.
[17] J. Kim, J.E. Dick, A.J. Bard, Advanced Electrochemistry of Individual Metal Clusters Electrodeposited Atom by Atom to Nanometer by Nanometer, Acc. Chem. Res. 49 (11) (2016) 2587–2595.
[18] C. Liu, P. Peljo, X. Huang, W. Cheng, L. Wang, H. Deng, Single Organic Droplet Collision Voltammogram via Electron Transfer Coupled Ion Transfer, Anal. Chem. 89 (17) (2017) 9284–9291.
[19] J.E. Dick, A.J. Bard, Toward the Digital Electrochemical Recognition of Cobalt, Iridium, Nickel, and Iron Ion Collisions by Catalytic Amplification, J. Am. Chem. Soc. 138 (27) (2016) 8446–8452.
[20] J.E. Dick, A.J. Bard, Recognizing Single Collisions of $PtCl_6^{2-}$ at Femtomolar Concentrations on Ultramicroelectrodes by Nucleating Electrocatalytic Clusters, J. Am. Chem. Soc. 137 (43) (2015) 13752–13755.
[21] J.B. Sambur, P. Chen, Distinguishing Direct and Indirect Photoelectrocatalytic Oxidation Mechanisms Using Quantitative Single-Molecule Reaction Imaging and Photocurrent Measurements, J. Phys. Chem. C 120 (37) (2016) 20668–20676.
[22] P. Chen, X. Zhou, H. Shen, N.M. Andoy, E. Choudhary, K.-S. Han, G. Liu, W. Meng, Single-molecule fluorescence imaging of nanocatalytic processes, Chem. Soc. Rev. 39 (12) (2010) 4560–4570.
[23] M. Pumera, Impact Electrochemistry: Measuring Individual Nanoparticles, ACS Nano 8 (8) (2014) 7555–7558.
[24] E.J.E. Stuart, K. Tschulik, C. Batchelor-McAuley, R.G. Compton, Electrochemical Observation of Single Collision Events: Fullerene Nanoparticles, ACS Nano 8 (8) (2014) 7648–7654.
[25] F.T. Patrice, K. Qiu, Y.-L. Ying, Y.-T. Long, Single Nanoparticle Electrochemistry, Annu. Rev. Anal. Chem. 12 (1) (2019) 347–370.
[26] M.V. Mirkin, T. Sun, Y. Yu, M. Zhou, Electrochemistry at One Nanoparticle, Acc. Chem. Res. 49 (10) (2016) 2328–2335.
[27] W. Xu, G. Zou, H. Hou, X. Ji, Single Particle Electrochemistry of Collision, Small 15 (32) (2019) 1804908, https://doi.org/10.1002/smll.v15.3210.1002/smll.201804908.
[28] R.A. Crane, T.B. Scott, Nanoscale zero-valent iron: Future prospects for an emerging water treatment technology, J. Hazard. Mater. 211–212 (2012) 112–125.
[29] S.M. Ponder, J.G. Darab, T.E. Mallouk, Remediation of Cr(VI) and Pb(II) Aqueous Solutions Using Supported, Nanoscale Zero-valent Iron, Environ. Sci. Technol. 34 (12) (2000) 2564–2569.
[30] J. Adusei-Gyamfi, V. Acha, Carriers for nano zerovalent iron (nZVI): synthesis, application and efficiency, RSC Adv. 6 (93) (2016) 91025–91044.
[31] T. Pasinszki, M. Krebsz, Synthesis and Application of Zero-Valent Iron Nanoparticles in Water Treatment, Environmental Remediation, Catalysis, and Their Biological Effects, Nanomaterials 10(5) (2020) 917 1-37.
[32] C. Fajardo, L.T. Ortíz, M.L. Rodríguez-Membibre, M. Nande, M.C. Lobo, M. Martin, Assessing the impact of zero-valent iron (ZVI) nanotechnology on soil microbial structure and functionality: A molecular approach, Chemosphere 86 (8) (2012) 802–808.
[33] Y.S. El-Temsah, D.H. Oughton, E.J. Joner, Effects of nano-sized zero-valent iron on DDT degradation and residual toxicity in soil: a column experiment, Plant Soil 368 (1) (2013) 189–200.
[34] M. Gil-Díaz, L.T. Ortiz, G. Costa, J. Alonso, M.L. Rodríguez-Membibre, S. Sánchez-Fortún, A. Pérez-Sanz, M. Martín, M.C. Lobo, Immobilization and Leaching of Pb and Zn in an Acidic Soil Treated with Zerovalent Iron Nanoparticles (nZVI): Physicochemical and Toxicological Analysis of Leachates, Water Air Soil Poll. 225 (6) (2014) 1990 1-13.
[35] W.-X. Zhang, Nanoscale Iron Particles for Environmental Remediation: An Overview, J. Nanopart. Res. 5 (3) (2003) 323–332.
[36] N. Ghosh, B.K. Mandal, K. Mohan Kumar, Magnetic memory effect in chelated zero valent iron nanoparticles, J. Magn. Magn. Mater. 324 (22) (2012) 3839–3841.
[37] Y.-P. Sun, X.-Q. Li, J. Cao, W.-X. Zhang, H.P. Wang, Characterization of zero-valent iron nanoparticles, Adv. Colloid Interface Sci. 120 (1-3) (2006) 47–56.
[38] D.J. Miller, M.C. Biesinger, N.S. McIntyre, Interactions of CO_2 and CO at fractional atmosphere pressures with iron and iron oxide surfaces: one possible mechanism for surface contamination?, Surf. Interface Anal. 33 (4) (2002) 299–305.
[39] K. Tschulik, B. Haddou, D. Omanović, N.V. Rees, R.G. Compton, Coulometric sizing of nanoparticles: Cathodic and anodic impact experiments open two independent routes to electrochemical sizing of Fe_3O_4 nanoparticles, Nano Res. 6 (11) (2013) 836–841.
[40] P. Ghods, O.B. Isgor, J.R. Brown, F. Bensebaa, D. Kingston, XPS depth profiling study on the passive oxide film of carbon steel in saturated calcium hydroxide solution and the effect of chloride on the film properties, Appl. Surf. Sci. 257 (10) (2011) 4669–4677.
[41] K.T. Soto Hidalgo, R. Guzmán-Blas, E.O. Ortiz-Quiles, E.R. Fachini, J. Corchado-García, E. Larios, B. Zayas, M. José-Yacamán, C.R. Cabrera, Highly organized nanofiber formation from zero valent iron nanoparticles after cadmium water remediation, RSC Adv. 5 (4) (2015) 2777–2784.
[42] K.T. Soto Hidalgo, P.J. Carrión-Huertas, R.T. Kinch, L.E. Betancourt, C.R. Cabrera, Phytonanoremediation by Avicennia Germinans (black mangrove) and Nano Zero Valent Iron for Heavy Metal Uptake from Cienaga Las Cucharillas Wetland Soils, Environ. Nanotechnol. Monit. Manag. 14 (100363) (2020) 1–9.
[43] J.F. Moulder, W.F. Stickle, P.E. Sobol, K.D. Bomben, Handbook of X-ray Photoelectron Spectroscopy, Physical Electronics (1992) 80–81.
[44] O. Milkovič, J. Gamcová, M. Sopko, I. Škorvánek, Structure and Magnetic Properties of Iron/Iron-Oxide Nanoparticles Prepared by Precipitation from Solid State Solution, Acta Phys. Pol. A 131 (4) (2017) 747–749.
[45] L.A. Grunes, R.D. Leapman, C.N. Wilker, R. Hoffmann, A.B. Kunz, Oxygen K near-edge fine structure: An electron-energy-loss investigation with comparisons to new theory for selected 3d Transition-metal oxides, Phys. Rev. B 25 (12) (1982) 7157–7173.
[46] R.D. Leapman, L.A. Grunes, Anomalous L_3/L_2 White-Line Ratios in the *3d* Transition Metals, Phys. Rev. Lett. 45 (5) (1980) 397–401.
[47] R.D. Leapman, L.A. Grunes, P.L. Fejes, Study of the $L_{2,3}$ edges in the *3d* transition metals and their oxides by electron-energy-loss spectroscopy with comparisons to theory, Phys. Rev. B 26 (2) (1982) 614–635.
[48] M. Pourbaix, Atlas of Electrochemical Equilibria in Aqueous Solutions, in: TX, 2nd Edition., National Association of Corrosion Engineers, Houston, 1974, pp. 307–321.
[49] A. Einstein, Zur Elektrodynamik bewegter Körper, Ann. Phys. 322 (10) (1905) 891–921.